Prediction of new topological superconductor candidate $1T$-Ti(Se$_{1-y}$Te$_y$)$_2$

Wenjun Liu, Aiyun Luo, Guyue Zhong, Jinyu Zou, and Gang Xu[*]

Wuhan National High Magnetic Field Center and School of Physics, Huazhong University of Science and Technology, Wuhan 430074, China

Topological superconductivity has attracted intensive interest for its ability to host the Majorana zero mode and its implementation in topological quantum computations. Based on first-principles calculations and the analysis of the effective Bogoliubov–de Gennes Hamiltonian, we demonstrate that $1T$-TiTe$_2$ is a topological metal hosting topological surface states near the Fermi level, and it exhibits a normal-topological-normal superconducting phase transition as a function of the chemical potential. These results point to a new promising topological superconductor. Furthermore, our calculations also suggest that the transition metal intercalated Ti(Se$_{1-y}$Te$_y$)$_2$ is also a highly possible route to realize topological superconductivity and Majorana zero modes.

I. INTRODUCTION

As one of the most intriguing systems to host Majorana zero modes (MZMs), topological superconductors (TSCs) play important roles in both condensed matter physics and topological quantum computations [1–3], which have attracted growing interest in the past decade [4–6]. Since natural TSCs are very rare [7–9], a variety of architectures have been proposed in one, two, and three dimensions for the realization of TSCs and MZMs [10–27]. In particular, Xu *et al.* proposed that a TSC can be realized in the vortex of superconducting topological metallic materials such as the iron-based superconductor FeSe$_{0.5}$Te$_{0.5}$ [24]. Recently, MZMs and superconducting gaps on the surface states have been observed in Fe(Se,Te) [28–30] and (Li$_{0.84}$Fe$_{0.16}$)OHFeSe [31]. Such exciting progress promotes superconducting topological metallic materials to the forefront of exploring MZMs and topological qubits [16,20].

Titanium dichalcogenides ($1T$-TiX_2, $X =$ Se, Te) have attracted much attention due to their intriguing emergent phenomena, including topological states [32,33], superconductivity [34–36], and charge density waves [37–43], which make such a system a promising platform to explore these interesting physics and their interplay. Both angle-resolved photoemission spectroscopy (ARPES) experiments and first-principles calculations have confirmed that $1T$-TiTe$_2$ and $1T$-TiSe$_2$ are semimetals [44–46]. Experimentally, both pressure in $1T$-TiTe$_2$ [36] or transition metal intercalation in $1T$-TiSe$_2$ [47] can suppress the charge density wave transition and induce superconductivity. In addition, $1T$-TiTe$_2$ is often used to characterize the electronic structure of the superconductor $1T$-Cu$_x$TiSe$_2$ [48]. The interest in $1T$-TiTe$_2$ is continuously increasing in view of the evidence about pressure-induced topological phase transitions [49,50], creating the prospect to explore the emergence of TSCs and MZMs in this material.

In this paper, by means of first-principles calculations, we demonstrate that the layered titanium dichalcogenide $1T$-TiTe$_2$ is a pressure-induced superconducting topological metal. Its band structures manifest a *p-d* band inversion and a topologically nontrivial gap near the Fermi level. Topological surface states could be stabilized on a (001) surface. When $1T$-TiTe$_2$ enters the superconducting phase under about 5–12 GPa [36], the calculated energy spectrum of the vortex Bogoliubov–de Gennes (BdG) Hamiltonian exhibits a normal-topological-normal superconducting phase transition. Considering that a topologically nontrivial band gap tends to shift towards the Fermi level by applying uniaxial pressure, we propose that $1T$-TiTe$_2$ is a promising TSC candidate. Further studies suggest that the transition metal intercalated Ti(Se$_{1-y}$Te$_y$)$_2$ is also a highly possible route to realize TSC and MZMs.

II. CRYSTAL STRUCTURE AND METHODOLOGY

As shown in Fig. 1(a), $1T$-TiTe$_2$ adopts a triangular lattice structure with space group $P\bar{3}m1$ (No. 164) [51], in which each layer of the Ti atom is surrounded by two layers of Te atoms, which forms a stable TiTe$_2$-octahedral sandwich. The TiTe$_2$-octahedral sandwiches are *A-A* stacked along the *c* axis, which finally constructs a layered van der Waals material. It undergoes a charge density wave transition at room temperature [37,38]. When an external pressure of about 5–12 GPa is applied, the charge density wave transition is suppressed, and a superconducting phase with the highest $T_c = 5.3$ K is induced [36]. The optimized crystal parameters $a = 3.84$ Å, $c = 6.68$ Å, and $z = 0.251$, which agree well with the experimental results, are used in our calculations. Our first-principles calculations are performed by the Vienna *ab initio* simulation package [52,53] based on the density functional
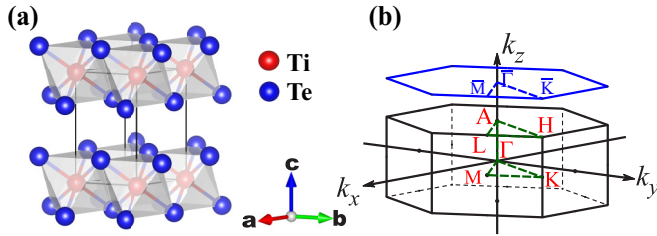
_____

[*]gangxu@hust.edu.cn

FIG. 1. (a) The crystal structure of $1T$-TiTe$_2$ in space group $P\bar{3}m1$. (b) High-symmetry k points in the bulk Brillouin zone and their projection on the (001) surface.

theory (DFT) and projected augmented-wave method [54]. The energy cutoff is set as 400 eV, and $11 \times 11 \times 9$ k meshes are adopted. The Perdew-Burke-Ernzerhof type of exchange-correlation potential [55], and the Heyd-Scuseria-Ernzerhof (HSE06) hybrid functional [56] with a Hartee-Fock exchange factor 0.2 are used in all calculations to obtain accurate electronic structures. The spin-orbit coupling (SOC) interaction is considered consistently.

III. FIRST-PRINCIPLES CALCULATIONS

In Figs. 2(a) and 2(b), we calculate and compare the band structures of $1T$-TiSe$_2$ and $1T$-TiTe$_2$, respectively. For both of them, two valence bands are not fully occupied, leading to two hole Fermi pockets around the Γ-A path, and one conduction band is partially occupied, leading to one electron Fermi pocket around the L point. Such semimetallic characteristics agree well with many ARPES observations [44,57,58], which confirm the validity of our calculation method. The
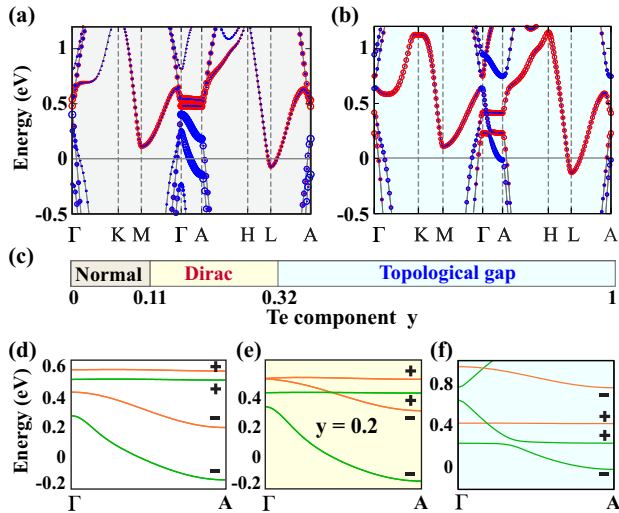

FIG. 2. Band structures of (a) $1T$-TiSe$_2$ and (b) $1T$-TiTe$_2$ from HSE06 calculations. The sizes of the red and blue circles represent the weight projections for the d orbitals of Ti atoms and the p orbitals of chalcogen atoms, respectively. (c) The topological phase diagram of Ti(Se$_{1-y}$Te$_y$)$_2$. (d)–(f) are the band structures along the Γ-A path of TiSe$_2$, Ti(Se$_{0.8}$Te$_{0.2}$)$_2$, and TiTe$_2$, respectively, in which we use orange and green bands to denote the $j_{\text{eff}}^z = \pm 3/2$ states and $j_{\text{eff}}^z = \pm 1/2$ states. The even/odd ($+/-$) parity for each band at the A point is also marked in (d)–(f).

orbital projections illustrate that the valence bands are mostly contributed by the p orbitals ($p_x \& p_y$) of the chalcogen atoms, while the conduction bands are mostly from the d orbitals (d_{z^2} around the L point) of Ti atoms. These results are consistent with a previous analysis that charge transfer occurs from titanium to chalcogen, and verify that the Ti ion has a chemical valence close to +4 [59]. Moreover, we notice that two conduction bands with even parity contributed by the d orbitals ($d_{xz} \& d_{yz}$) are just 78 meV higher than the valence-band top (odd parity) at Γ in $1T$-TiSe$_2$, as shown in Fig. 2(a). If the energy of the d bands can be modulated a little lower, p-d band inversion could occur along the Γ-A path. This is exactly what happened in $1T$-TiTe$_2$. As shown in Fig. 2(b), the p-d band overlap is enhanced drastically when the Se atoms are substituted by the Te atoms. As a result, one upper p band is pushed above the d bands along the Γ-A path, and one lower p band intersects with the $d_{xz} \& d_{yz}$ bands, forming the p-d band inversion along the Γ-A path. Therefore, $1T$-TiTe$_2$ becomes a topological metal [50], which is very similar to the band structures of the Fe(Se,Te) [24,60].

These results suggest that the topological metal phase can be engineered by doping Te to $1T$-TiSe$_2$ [59]. We thus perform virtual crystal approximation (VCA) calculations on the band structures of Ti(Se$_{1-y}$Te$_y$)$_2$. The calculated results give rise to three phases depending on the Te component y, as shown in Fig. 2(c). When y is less than 0.11, the d bands with even parity are always higher than the p bands with odd parity, and the system falls into the normal metal phase as represented in Figs. 2(a) and 2(d). As the Te component y increases, the chemical bonding between the p and d orbitals is weakened because the electronegativity of Te is smaller than that of Se. Consequently, the d bands are pushed lower and lower, and the system enters the Dirac semimetal phase at $0.11 < y < 0.32$, as represented by the band structures of Ti(Se$_{0.8}$Te$_{0.2}$)$_2$ in Fig. 2(e). When y is large than 0.32, the band inversion is further enhanced. A topologically nontrivial band gap appears near the Fermi level, accompanied by a three-dimensional Dirac cone at higher energy, as shown in Figs. 2(b) and 2(f). We call these band structures the "topological gap" phase in Fig. 2(c).

To understand the whole phase diagram in Fig. 2(c), we should take into account the SOC interaction and analyze the C_{3z} irreducible representation of each band along the Γ-A path. As shown in Figs. 2(d)–2(f), our calculations demonstrate that the ($p_x \& p_y$) orbitals and ($d_{xz} \& d_{yz}$) orbitals always split into the same j_{eff}^z order by SOC interaction, i.e., $j_{\text{eff}}^z = \pm 3/2$ states [orange bands in Figs. 2(d)–2(f)] are higher than the $j_{\text{eff}}^z = \pm 1/2$ states [green bands in Figs. 2(d)–2(f)] for both p and d orbitals. This seems contradictory to the conventional knowledge that d orbitals have a negative SOC interaction with respect to that of the p orbitals [61–63]. But it is a reasonable result due to the strong p-d hybridization that has been confirmed in many other materials [64–66]. Once the ordering is aligned as in Figs. 2(d)–2(f), the $d_{\pm 1/2}$ states will invert with the $p_{\pm 3/2}$ states first as the p-d band overlap increases. Due to the C_{3z} protection [67,68], this band inversion leads to a pair of stable Dirac points rather than a nontrivial band gap on the Γ-A line as shown in Fig. 2(e). Only when y exceeds 0.32 will the $d_{\pm 1/2}$ states be able to invert with the $p_{\pm 1/2}$ states, and a nontrivial band gap can

be opened, leading to a topological metal phase as shown in Fig. 2(f).

IV. EFFECTIVE MODEL

Based on the DFT results, the bases describing the low-energy bands along the Γ-A path can be simplified as

$$
\begin{aligned}
|\phi_1\rangle_+ &= (d_{xz} + id_{yz})/\sqrt{2}, \\
|\phi_2\rangle_+ &= (d_{xz} - id_{yz})/\sqrt{2}, \\
|\phi_3\rangle_- &= (p_x + ip_y)/\sqrt{2}, \\
|\phi_4\rangle_- &= (p_x - ip_y)/\sqrt{2},
\end{aligned}
\tag{1}
$$

where the subscripts $\pm$ denote the parity of the basis. As we discussed above, the band inversion between $|\phi_{1,2}\rangle$ and $|\phi_{3,4}\rangle$ along the Γ-A path could lead to the topologically nontrivial band structures in $1T$-TiTe$_2$. The effective model at the Γ point has the full point group symmetry D_{3d} of the crystal with the generator of rotation C_{3z}, inversion I, and mirror M_x. Under the constraint of D_{3d} and time-reversal symmetry, the effective Hamiltonian without SOC is restricted to the following form,

$$
H_0(k) = \begin{pmatrix}
M_d(k) & 0 & it_1 f(k_z) & t_2 k_+ \\
0 & M_d(k) & -t_2 k_- & it_1 f(k_z) \\
-it_1 f(k_z) & -t_2 k_+ & M_p(k) & 0 \\
t_2 k_- & -it_1 f(k_z) & 0 & M_p(k)
\end{pmatrix},
\tag{2}
$$

with

$$
M_i = E_i + t_i^{//}(k_x^2 + k_y^2) + t_i^z g(k_z), \quad i = d, p,
\tag{3}
$$

and

$$
\begin{aligned}
f(k_z) &= \sin(ck_z), \\
g(k_z) &= 1 - \cos(ck_z).
\end{aligned}
\tag{4}
$$

where $E_{d,p}$ are the band energies of $d_{xz\&yz}$ and $p_{x\&y}$ orbitals at the Γ point, and $t_i^{//}$ and t_i^z are the in-plane and z-direction hopping amplitudes of the ith band. c is the lattice constant along the z direction. t_1 and t_2 are the couplings between p and d orbitals.

The full Hamiltonian with SOC takes the form $H(k) = I \otimes H_0(k) + H_{\text{SOC}}$ under the spinful bases $(|\uparrow\rangle, |\downarrow\rangle) \otimes (|\phi_1\rangle, |\phi_2\rangle, |\phi_3\rangle, |\phi_4\rangle)$. The symmetry-allowed H_{SOC} is given explicitly by Eqs. (S1)–(S3) [see details in Sec. I of the Supplemental Material (SM) [69]]. Four new parameters induced by the SOC interaction are considered. $\lambda_{d,p}$ are the on-site SOC strengths for d and p orbitals, respectively. λ_1 is the first-order SOC induced by the z-direction hopping of the p orbitals, and λ_2 is induced by the in-plane hopping between the p and d orbitals with opposite spin [69].

We use the effective model to fit the DFT calculated band structures of $1T$-TiTe$_2$, and list the fitted parameters in Table I. The fitted band structures (red) are plotted in Figs. 3(a)–3(c), which show that our model and parameters successfully capture the band dispersions and topological characters of the $1T$-TiTe$_2$ along the Γ-A path. Especially, a topologically nontrivial band gap with amplitude 36 meV is opened at about

TABLE I. Parameters in the effective model.

E_d (eV)	E_p (eV)	t_1 (eV)	t_2 (eV Å)	$t_d^{//}$ (eV Å^2)	$t_p^{//}$ (eV Å^2)
0.324	0.789	0.046	3.1	7.5	−7.0
t_d^z (eV)	t_p^z (eV)	λ_d (eV)	λ_p (eV)	λ_1 (eV)	λ_2 (eV Å)
0.001	−0.211	0.094	0.154	0.113	2.0

0.24 eV above the Fermi level, and a Dirac point presents at about 0.4 eV above the Fermi level, as shown in Fig. 3(a). As shown in Figs. 3(b) and 3(c), the in-plane band dispersions below 0.5 eV are reproduced reasonably well. The mismatch parts are mainly contributed by the d_{z^2} orbital (blue bands in Fig. 3), which has not been considered in our effective model. However, we notice that the topological properties of the band structures are not determined by the d_{z^2} band. It also does not influence the phase diagram of the topological superconductivity, because it is mainly dominated by the low-energy physics at the Γ and A points [24,70].

We note that, to describe the band dispersions along the Γ-A direction well, the effective model has been written as a combination of an in-plane $k \cdot p$ model and a z-direction tight-binding model, as is the case in the topological superconducting system FeSe$_{0.5}$Te$_{0.5}$ [24]. To perform the (001) surface calculations based on the effective model, we construct a finite thickness slab geometry along the z direction while keeping the in-plane $k \cdot p$ form, where the interactions between neighbor layers are described by the tight-binding hopping parameters [71]. The calculated results are shown in Fig. 3(d), in which two branches of topological surface states cross each other at about 0.235 eV as highlighted by red and blue bands, respectively. We note that the topological surface states crossing in TiTe$_2$ are more like those in LiFeAs [72] than those in FeSe$_{0.5}$Te$_{0.5}$ [24]. In Fig. S1 [69], we plot the real-space charge density distribution of the surface states as illustrated by the dark gray square in Fig. 3(d), which are mainly distributed on the surface within 10 Å and show an exponential decay with the depth. These results successfully
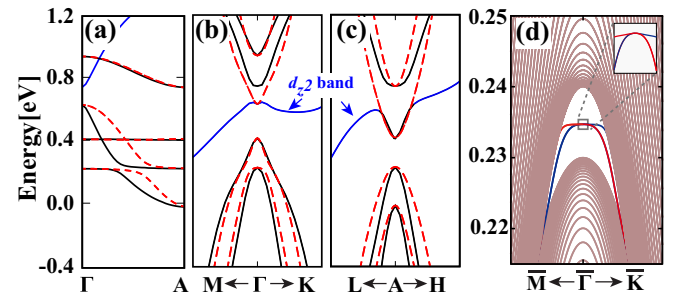

FIG. 3. (a)–(c) show the fitted band structures from the effective model (dashed red bands) with the DFT calculations (solid black and blue bands) along the high-symmetry k path. The blue bands are mostly contributed by the d_{z^2} orbital, which are not considered in our effective model. (d) The (001) surface states calculated by the effective Hamiltonian, where the inset shows a closeup view of the topological surface states crossing clearly. In all figures, the Fermi level is set at 0 eV.

confirm the topological electronic properties of our model in TiTe$_2$.

V. TOPOLOGICAL SUPERCONDUCTIVITY

Considering 1T-TiTe$_2$ is a superconductor under a pressure of about 5–12 GPa, we would like to study the possible TSC phase realized in it in the following. Since the crystal structure and the topological band structures along Γ-A change slightly under pressure [49], the parameters in Table I are used to describe the band structures of 1T-TiTe$_2$ under pressure. Similar to Fe(Se,Te) [24], 1T-TiTe$_2$ is a type-II superconductor. When the superconducting 1T-TiTe$_2$ is in an external magnetic field, the magnetic flux would penetrate into the superconductor and form many vortex lines in the sample [36]. Thus, one can view the vortex line as a Majorana chain, and study its BdG spectrum to determine the whole system's topological properties [1,70].

Since the magnetic field is usually very weak in the vortex lines, we ignore the vector potential $A(r)$ and the Zeeman effect in the type-II limit [73,74]. Then the BdG Hamiltonian of the vortex can be written as

$$H_{BdG}(r,\theta) = \begin{pmatrix} H'(k) - \mu & \Delta e^{-i\theta} \tanh(r/\xi) \\ \Delta e^{i\theta} \tanh(r/\xi) & -H'^*(-k) + \mu \end{pmatrix}. \quad (5)$$

Here, the vortex is assumed along the z direction. $H'(k)$ is the eight-band Hamiltonian obtained from $H(k)$ by a unitary transformation [69]. μ is the chemical potential, and (r,θ) are the polar coordinates in the xy plane. $\xi = 3.6$ nm is the Ginzburg-Landau coherent length [36]. A uniform s-wave superconducting pairing is adopted by assuming $\Delta = \Delta_0(i\tau_y \otimes I_4)$ with $\Delta_0 = 1.2$ meV [36], where I_4 is a 4×4 identity matrix, and τ_y is the second Pauli matrix.

For the Majorana chain described by Eq. (5), only k_z is the good quantum number, and its topological phase transition can only be characterized by a gap closing of the BdG spectrum at either $k_z = 0$ (Γ) or $k_z = \pi$ (A) [70]. Therefore, by discretizing the polar coordinate r on a cylinder with the radius 3.6 μm, we numerically solve the vortex BdG Hamiltonian, and plot the spectra at the A and the Γ points as functions of the chemical potential μ in Figs. 4(a) and 4(b), respectively. The calculated results obviously manifest that the spectrum at the A point is always gapped, while the energy spectrum at the Γ point closes its gap at the critical chemical potentials $\mu_{c1} = 266$ meV and $\mu_{c2} = 293$ meV. Considering the bulk pairing dominates at the chemical potential far away from the Dirac point, our results strongly suggest that the vortex line falls into the normal superconductivity (NSC) phase both for $\mu < 266$ meV and $\mu > 293$ meV, and the TSC phase is realized in the chemical potential interval $\mu \in [\mu_{c1}, \mu_{c2}]$. We note that the energy interval $\mu \in [\mu_{c1}, \mu_{c2}]$ does not exactly correspond to the energy window of topological surface states shown in Fig. 3(d). Such a shift has been reported and explained previously [75].

In Figs. 4(c)–4(e) we plot the BdG spectrum of the vortex line at different chemical potentials in the NSC phase [$\mu = 245$ meV for Fig. 4(c)], at the phase transition point [$\mu = 266$ meV for Fig. 4(d)], and in the TSC phase [$\mu = 280$ meV for Fig. 4(e)], respectively. They clearly show a gap closing and reopening process at the Γ point as μ is
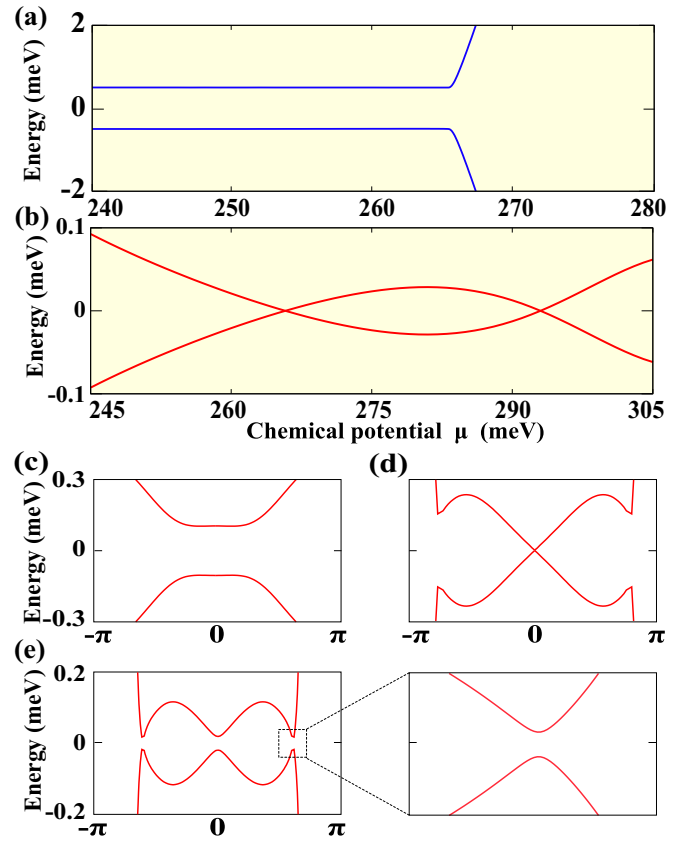

FIG. 4. (a) and (b) are the energy spectra of the vortex lines at the A and the Γ points as a function of chemical potential μ, respectively. While the spectrum is always gapped at the A point, the energy spectrum at the Γ point shows two gap closings at the critical chemical potentials 266 and 293 meV. (c)–(e) are the low-energy dispersions of the BdG Hamiltonian of the vortex line for the NSC phase [(c) with $\mu = 245$ meV], the critical point of the phase transition [(d) with $\mu = 266$ meV)], and the TSC phase [(e) with $\mu = 280$ meV], respectively.

varied. In particular, the spectrum beside the transition point is fully gapped at all k_z, which is the crucial requirement to protect stable MZMs at the vortex ends. As we know, the Zak phase is a well-defined topological number to characterize the topological property of the 1D superconductor as the gap is opened [76,77]. We notice that, different from the Fe(Se,Te), the gap closing point of the chemical potential in 1T-TiTe$_2$ is not affected by the bulk superconducting gap Δ_0, as shown in Fig. S2(a). More importantly, the gap size at fixed μ is increased monotonously with Δ_0 as shown in Fig. S2(b). Taking advantage of these properties, we can calculate the Zak phase at large Δ_0 to determine the real TSC region in 1T-TiTe$_2$. We have calculated the evolution of the Zak phase as a function of μ with $\Delta_0 = 50$ meV, which manifests that the Zak phase is 0 at the beginning ($\mu < 267$ meV), and rises to π at $\mu \in [267$ meV, 291 meV], and finally turns back to 0 as $\mu > 291$ meV as shown in Fig. S2(c). These results verify that the vortex chain in 1T-TiTe$_2$ falls into the TSC phase as $\mu \in [\mu_{c1}, \mu_{c2}]$ [24,70]. Our results also suggest that, similar to the TSC phase in Cu$_x$Bi$_2$Se$_3$ [12,70], one can improve the stability of the TSC phase and enhance the critical temperature
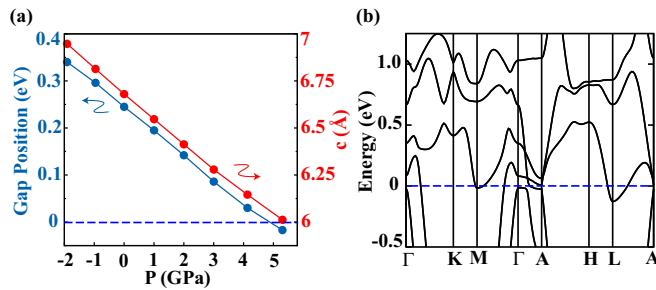
FIG. 5. The electronic structures of $1T$-TiTe$_2$ under uniaxial pressure along the c axis. (a) The energy position of the topologically nontrivial gap (dark blue) and the length of the c axis (red) as a function of uniaxial pressure along the c axis. The topologically nontrivial gap indicates a band gap between the valence top and the conduction bottom along the Γ-A direction. (b) The electronic band structures of $1T$-TiTe$_2$ under a uniaxial pressure of about 5.3 GPa. The blue dashed line represents the Fermi level.

of MZMs in $1T$-TiTe$_2$ by increasing its bulk superconducting gap, which is another advantage that the TSC phases in iron-based superconductors do not have.

VI. DISCUSSION

The pressure can not only bring out superconductivity in $1T$-TiTe$_2$, but it also can adjust its band structures [32,35,36,49,50]. According to Ref. [35], uniaxial pressure can even enhance its superconductivity. Therefore, we would like to simulate the evolution of the electronic structures of $1T$-TiTe$_2$ by applying uniaxial pressure along the c axis, where the c axis reduces under pressure while the in-plane lattices expand with Poisson's ratio $\nu = -\Delta a/\Delta c = 0.23$. The calculated results are summarized in Fig. 5(a), which demonstrates that the energy position of the topologically nontrivial gap moves down monotonically (blue points) with increasing

uniaxial pressure, and reaches the Fermi level at about 5 GPa. In Fig. 5(b), we plot the electronic band structures under a uniaxial pressure of about 5.3 GPa, in which the topologically nontrivial band gap is moved to about -17 meV. Roughly, if we assume that the chemical potential interval of TSC moves with the topological band gap correspondingly, the superconducting $1T$-TiTe$_2$ under 5.3 GPa pressure could fall into the TSC phase between $\mu \in [-3$ meV, 21 meV]. These results demonstrate that $1T$-TiTe$_2$ under modest uniaxial pressure has a big chance of hosting TSC at the Fermi level.

Finally, we would like to discuss another highly possible route to realize TSC in titanium dichalcogenides. As we know, some transition metal intercalation can also suppress the charge density wave transition, and induce superconductivity in $1T$-TiSe$_2$. For example, a $T_c = 4$ K superconductivity transition has been observed in Cu-intercalated $1T$-TiSe$_2$ [47]. According to our calculations, Te-doped $1T$-TiSe$_2$ has very similar band structures with TiTe$_2$, including the p-d band inversion and a topological gap as shown in Fig. S3. Moreover, such Te doping can enhance the density of states at the Fermi level, which is beneficial for superconductivity [78]. Therefore, one can expect that TSC and MZMs can be realized in the Te-doped Cu$_x$TiSe$_2$ system. Taking the half-doped $1T$-TiSe$_2$ as a concrete example, we have calculated its band structures as shown in Fig. S3(a) by using the VCA. The corresponding spectrum for the vortex BdG model with $\Delta_0 = 0.8$ meV is plotted in Fig. S4, which exhibits a similar spectrum gap closing behavior as in $1T$-TiTe$_2$. These results demonstrate that Te-doped $1T$-TiSe$_2$ is also a promising TSC candidate at the VCA level, where the inhomogeneity induced by Te substitution is neglected.

[1] A. Y. Kitaev, Unpaired Majorana fermions in quantum wires, Phys. Usp. **44**, 131 (2001).

[2] A. Kitaev, Fault-tolerant quantum computation by anyons, Ann. Phys. **303**, 2 (2003).

[3] N. Read and D. Green, Paired states of fermions in two dimensions with breaking of parity and time-reversal symmetries and the fractional quantum Hall effect, Phys. Rev. B **61**, 10267 (2000).

[4] S. D. Sarma, M. Freedman, and C. Nayak, Majorana zero modes and topological quantum computation, npj Quantum Inf. **1**, 15001 (2015).

[5] M. Sato and Y. Ando, Topological superconductors: A review, Rep. Prog. Phys. **80**, 076501 (2017).

[6] R. M. Lutchyn, E. P. A. M. Bakkers, L. P. Kouwenhoven, P. Krogstrup, C. M. Marcus, and Y. Oreg, Majorana zero modes in superconductor–semiconductor heterostructures, Nat. Rev. Mater. **3**, 52 (2018).

[7] A. P. Mackenzie, T. Scaffidi, C. W. Hicks, and Y. Maeno, Even odder after twenty-three years: the superconducting

order parameter puzzle of Sr$_2$RuO$_4$, npj Quantum Mater. **2**, 40 (2017).

[8] M. Sakano, K. Okawa, M. Kanou, H. Sanjo, T. Okuda, T. Sasagawa, and K. Ishizaka, Opologically protected surface states in a centrosymmetric superconductor β-dBi$_2$, Nat. Commun. **6**, 8595 (2015).

[9] Y. Li, H. Zheng, Y. Fang, D. Zhang, Y. Chen, C. Chen, A. Liang, W. Shi, D. Pei, L. Xu *et al.*, Observation of topological superconductivity in a stoichiometric transition metal dichalcogenide 2M-WS$_2$, Nat. Commun. **12**, 2874 (2021).

[10] S. Das Sarma, C. Nayak, and S. Tewari, Proposal to stabilize and detect half-quantum vortices in strontium ruthenate thin films: Non-Abelian braiding statistics of vortices in a $p_x + ip_y$ superconductor, Phys. Rev. B **73**, 220502(R) (2006).

[11] C. Nayak, S. H. Simon, A. Stern, M. Freedman, and S. Das Sarma, Non-Abelian anyons and topological quantum computation, Rev. Mod. Phys. **80**, 1083 (2008).

[12] L. Fu and C. L. Kane, Superconducting Proximity Effect and Majorana Fermions at the Surface of a

Topological Insulator, Phys. Rev. Lett. **100**, 096407 (2008).

[13] K. T. Law, P. A. Lee, and T. K. Ng, Majorana Fermion Induced Resonant Andreev Reflection, Phys. Rev. Lett. **103**, 237001 (2009).

[14] J. D. Sau, S. Tewari, and S. Das Sarma, Universal quantum computation in a semiconductor quantum wire network, Phys. Rev. A **82**, 052322 (2010).

[15] J. D. Sau, R. M. Lutchyn, S. Tewari, and S. Das Sarma, Robustness of Majorana fermions in proximity-induced superconductors, Phys. Rev. B **82**, 094522 (2010).

[16] R. M. Lutchyn, J. D. Sau, and S. Das Sarma, Majorana Fermions and a Topological Phase Transition in Semiconductor-Superconductor Heterostructures, Phys. Rev. Lett. **105**, 077001 (2010).

[17] Y. Oreg, G. Refael, and F. von Oppen, Helical Liquids and Majorana Bound States in Quantum Wires, Phys. Rev. Lett. **105**, 177002 (2010).

[18] J. Alicea, Majorana fermions in a tunable semiconductor device, Phys. Rev. B **81**, 125318 (2010).

[19] A. C. Potter and P. A. Lee, Multichannel Generalization of Kitaev's Majorana End States and a Practical Route to Realize Them in Thin Films, Phys. Rev. Lett. **105**, 227003 (2010).

[20] J. Alicea, Y. Oreg, G. Refael, F. von Oppen, and M. P. A. Fisher, Non-Abelian statistics and topological quantum information processing in 1D wire networks, Nat. Phys. **7**, 412 (2011).

[21] M. Duckheim and P. W. Brouwer, Andreev reflection from non-centrosymmetric superconductors and Majorana bound-state generation in half-metallic ferromagnets, Phys. Rev. B **83**, 054513 (2011).

[22] H. Weng, G. Xu, H. Zhang, S.-C. Zhang, X. Dai, and Z. Fang, Half-metallic surface states and topological superconductivity in $NaCoO_2$ from first principles, Phys. Rev. B **84**, 060408(R) (2011).

[23] G. Xu, J. Wang, B. Yan, and X.-L. Qi, Topological superconductivity at the edge of transition-metal dichalcogenides, Phys. Rev. B **90**, 100505(R) (2014).

[24] G. Xu, B. Lian, P. Tang, X.-L. Qi, and S.-C. Zhang, Topological Superconductivity on the Surface of Fe-Based Superconductors, Phys. Rev. Lett. **117**, 047001 (2016).

[25] J. Zou, Q. Xie, Z. Song, and G. Xu, New types of topological superconductors under local magnetic symmetries, Natl. Sci. Rev. **8**, nwaa169 (2020).

[26] X.-H. Pan, K.-J. Yang, L. Chen, G. Xu, C.-X. Liu, and X. Liu, Lattice-Symmetry-Assisted Second-Order Topological Superconductors and Majorana Patterns, Phys. Rev. Lett. **123**, 156801 (2019).

[27] L. Chen, B. Liu, G. Xu, and X. Liu, Lattice distortion induced first- and second-order topological phase transition in a rectangular high-T_c superconducting monolayer, Phys. Rev. Research **3**, 023166 (2021).

[28] J.-X. Yin, Z. Wu, J. Wang, Z. Ye, J. Gong, X. Hou, L. Shan, A. Li, X. Liang, X. Wu *et al.*, Observation of a robust zero-energy bound state in iron-based superconductor Fe(Te, Se), Nat. Phys. **11**, 543 (2015).

[29] T. Machida, Y. Sun, S. Pyon, S. Takeda, Y. Kohsaka, T. Hanaguri, T. Sasagawa, and T. Tamegai, Zero-energy vortex bound state in the superconducting topological surface state of Fe(Se, Te), Nat. Mater. **18**, 811 (2019).

[30] L. Kong, S. Zhu, M. Papaj, H. Chen, L. Cao, H. Isobe, Y. Xing, W. Liu, D. Wang, P. Fan, Y. Sun, S. Du, J. Schneeloch, R. Zhong, G. Gu, L. Fu, H.-J. Gao, and H. Ding, Half-integer level shift of vortex bound states in an iron-based superconductor, Nat. Phys. **15**, 1181 (2019).

[31] Q. Liu, C. Chen, T. Zhang, R. Peng, Y.-J. Yan, C.-H.-P. Wen, X. Lou, Y.-L. Huang, J.-P. Tian, X.-L. Dong, G.-W. Wang, W.-C. Bao, Q.-H. Wang, Z.-P. Yin, Z.-X. Zhao, and D.-L. Feng, Robust and Clean Majorana Zero Mode in the Vortex Core of High-Temperature Superconductor $(Li_{0.84}Fe_{0.16})OHFeSe$, Phys. Rev. X **8**, 041056 (2018).

[32] V. Rajaji, U. Dutta, P. C. Sreeparvathy, S. C. Sarma, Y. A. Sorb, B. Joseph, S. Sahoo, S. C. Peter, V. Kanchana, and C. Narayana, Structural, vibrational, and electrical properties of $1T − TiTe_2$ under hydrostatic pressure: Experiments and theory, Phys. Rev. B **97**, 085107 (2018).

[33] S.-M. Huang, S.-Y. Xu, B. Singh, M.-C. Hsu, C.-H. Hsu, C. Su, A. Bansil, and H. Lin, Aspects of symmetry and topology in the charge density wave phase of $1T − TiSe_2$, New J. Phys. **23**, 083037 (2021).

[34] A. F. Kusmartseva, B. Sipos, H. Berger, L. Forró, and E. Tutiš, Pressure Induced Superconductivity in Pristine $1T − TiSe_2$, Phys. Rev. Lett. **103**, 236401 (2009).

[35] R. Xiao, W. Lu, D. Shao, J. Li, M. Wei, H. Lv, P. Tong, X. Zhu, and Y. Sun, Manipulating superconductivity of $1T − TiTe_2$ by high pressure, J. Mater. Chem. C **5**, 4167 (2017).

[36] U. Dutta, P. S. Malavi, S. Sahoo, B. Joseph, and S. Karmakar, Pressure-induced superconductivity in semimetallic $1T − TiTe_2$ and its persistence upon decompression, Phys. Rev. B **97**, 060503(R) (2018).

[37] P. Chen, W. W. Pai, Y. H. Chan, A. Takayama, C. Z. Xu, A. Karn, S. Hasegawa, M. Y. Chou, S. K. Mo, A. V. Fedorov, and T. C. Chiang, Emergence of charge density waves and a pseudogap in single-layer $TiTe_2$, Nat. Commun. **8**, 516 (2017).

[38] S. Fragkos, R. Sant, C. Alvarez, A. Bosak, P. Tsipas, D. Tsoutsou, H. Okuno, G. Renaud, and A. Dimoulas, Room Temperature Commensurate Charge Density Wave in Epitaxial Strained $TiTe_2$ Multilayer Films, Adv. Mater. Interfaces **6**, 1801850 (2019).

[39] Y. I. Joe, X. Chen, P. Ghaemi, K. Finkelstein, G. de La Peña, Y. Gan, J. Lee, S. Yuan, J. Geck, G. MacDougall *et al.*, Emergence of charge density wave domain walls above the superconducting dome in $1T − TiSe_2$, Nat. Phys. **10**, 421 (2014).

[40] P. Chen, Y.-H. Chan, X.-Y. Fang, Y. Zhang, M.-Y. Chou, S.-K. Mo, Z. Hussain, A.-V. Fedorov, and T.-C. Chiang, Charge density wave transition in single-layer titanium diselenide, Nat. Commun. **6**, 8943 (2015).

[41] M.-K. Lin, J. A. Hlevyack, P. Chen, R.-Y. Liu, S.-K. Mo, and T.-C. Chiang, Charge Instability in Single-Layer $TiTe_2$ Mediated by van der Waals Bonding to Substrates, Phys. Rev. Lett. **125**, 176405 (2020).

[42] X.-Y. Fang, H. Hong, P. Chen, and T.-C. Chiang, X-ray study of the charge-density-wave transition in single-layer $TiSe_2$, Phys. Rev. B **95**, 201409(R) (2017).

[43] W.-M. Zhao, L. Zhu, Z. Nie, Q.-Y. Li, Q.-W. Wang, L.-G. Dou, J.-G. Hu, L. Xian, S. Meng, and S.-C. Li, Moiré enhanced charge density wave state in twisted $1T − TiTe_2/1T − TiSe_2$ heterostructures, Nat. Mater. **21**, 284 (2021).

[44] X.-F. Tang, Y.-X. Duan, F.-Y. Wu, S.-Y. Liu, C. Zhang, Y.-Z. Zhao, J.-J. Song, Y. Luo, Q.-Y. Wu, J. He, H. Y. Liu, W. Xu,

and J.-Q. Meng, Three-dimensional Fermi surface and electron-phonon coupling in semimetallic $1T-TiTe_2$ studied by angle-resolved photoemission spectroscopy, Phys. Rev. B **99**, 125112 (2019).

[45] S.-X. Zhu, C. Zhang, Q.-Y. Wu, X.-F. Tang, H. Liu, Z.-T. Liu, Y. Luo, J.-J. Song, F.-Y. Wu, Y.-Z. Zhao, S.-Y. Liu, T. Le, X. Lu, H. Ma, K.-H. Liu, Y.-H. Yuan, H. Huang, J. He, H. Y. Liu, Y.-X. Duan, and J.-Q. Meng, Temperature evolution of quasi-particle dispersion and dynamics in semimetallic $1T-TiTe_2$ via high-resolution angle-resolved photoemission spectroscopy and ultrafast optical pump-probe spectroscopy, Phys. Rev. B **103**, 115108 (2021).

[46] T. Jaouen, M. Rumo, B. Hildebrand, M.-L. Mottas, C. W. Nicholson, G. Kremer, B. Salzmann, F. Vanini, C. Barreteau, E. Giannini *et al.*, Unveiling the Semimetallic Nature of $1T-TiSe_2$ by Doping its Charge Density Wave, arXiv:1911.06053.

[47] E. Morosan, H. W. Zandbergen, B. S. Dennis, J. W. G. Bos, Y. Onose, T. Klimczuk, A. P. Ramirez, N. P. Ong, and R. J. Cava, Superconductivity in Cu_xTiSe_2, Nat. Phys. **2**, 544 (2006).

[48] J. F. Zhao, H. W. Ou, G. Wu, B. P. Xie, Y. Zhang, D. W. Shen, J. Wei, L. X. Yang, J. K. Dong, M. Arita, H. Namatame, M. Taniguchi, X. H. Chen, and D. L. Feng, Evolution of the Electronic Structure of $1T-Cu_xTiSe_2$, Phys. Rev. Lett. **99**, 146401 (2007).

[49] Q. Zhang, Y. Cheng, and U. Schwingenschlögl, Series of topo-logical phase transitions in $TiTe_2$ under strain, Phys. Rev. B **88**, 155317 (2013).

[50] M. Zhang, X. Wang, A. Rahman, Q. Zeng, D. Huang, R. Dai, Z. Wang, and Z. Zhang, Pressure-induced topological phase transitions and structural transition in $1T-TiTe_2$ single crystal, Appl. Phys. Lett. **112**, 041907 (2018).

[51] Y. Arnaud and M. Chevreton, Etude comparative des composés $TiX_2(X = S, Se, Te)$. Structures de $TiTe_2$ et TiSeTe, J. Solid State Chem. **39**, 230 (1981).

[52] G. Kresse and J. Furthmüller, Efficient iterative schemes for *ab initio* total-energy calculations using a plane-wave basis set, Phys. Rev. B **54**, 11169 (1996).

[53] G. Kresse and J. Furthmüller, Efficiency of ab-initio total energy calculations for metals and semiconductors using a plane-wave basis set, Comput. Mater. Sci. **6**, 15 (1996).

[54] P. E. Blöchl, Projector augmented-wave method, Phys. Rev. B **50**, 17953 (1994).

[55] J. P. Perdew, K. Burke, and M. Ernzerhof, Generalized Gra-dient Approximation Made Simple, Phys. Rev. Lett. **77**, 3865 (1996).

[56] J. Heyd, G. E. Scuseria, and M. Ernzerhof, Hybrid functionals based on a screened Coulomb potential, J. Chem. Phys. **118**, 8207 (2003).

[57] K. Rossnagel, L. Kipp, M. Skibowski, C. Solterbeck, T. Strasser, W. Schattke, D. Voß, P. Krüger, A. Mazur, and J. Pollmann, Three-dimensional Fermi surface determination by angle-resolved photoelectron spectroscopy, Phys. Rev. B **63**, 125104 (2001).

[58] T. V. Kuznetsova, A. N. Titov, Y. M. Yarmoshenko, E. Z. Kurmaev, A. V. Postnikov, V. G. Pleschev, B. Eltner, G. Nicolay, D. Ehm, S. Schmidt, F. Reinert, and S. Hüfner, High-resolution angle-resolved photoemission investigation of the electronic structure of Cr-intercalated $1T-TiTe_2$, Phys. Rev. B **72**, 085418 (2005).

[59] Z. Zhu, Y. Cheng, and U. Schwingenschlögl, Topological Phase Diagrams of Bulk and Monolayer $TiS_{2x}Te_x$, Phys. Rev. Lett. **110**, 077202 (2013).

[60] Z. Wang, P. Zhang, G. Xu, L. K. Zeng, H. Miao, X. Xu, T. Qian, H. Weng, P. Richard, A. V. Fedorov, H. Ding, X. Dai, and Z. Fang, Topological nature of the $FeSe_{0.5}Te_{0.5}$ superconductor, Phys. Rev. B **92**, 115119 (2015).

[61] K. Shindo, A. Morita, and H. Kamimura, Spin-Orbit Coupling in Ionic Crystals with Zincblende and Wurtzite Structures, J. Phys. Soc. Jpn. **20**, 2054 (1965).

[62] F. Virot, R. Hayn, M. Richter, and J. van den Brink, Metacinnabar (β-HgS): A Strong 3D Topological Insulator with Highly Anisotropic Surface States, Phys. Rev. Lett. **106**, 236806 (2011).

[63] X.-L. Sheng, Z.-M. Yu, R. Yu, H. Weng, and S. A. Yang, *d* Orbital Topological Insulator and Semimetal in the Antifluorite Cu_2S Family: Contrasting Spin Helicities, Nodal Box, and Hybrid Surface States, J. Phys. Chem. Lett. **8**, 3506 (2017).

[64] B. Tell and P. M. Bridenbaugh, Aspects of the band struc-ture of $CuGaS_2$ and $CuGaSe_2$, Phys. Rev. B **12**, 3330 (1975).

[65] K. Yoodee, J. C. Woolley, and V. Sa-yakanit, Effects of $p-d$ hybridization on the valence band of I-III-VI_2 chalcopyrite semiconductors, Phys. Rev. B **30**, 5904 (1984).

[66] X.-L. Sheng, Z. Wang, R. Yu, H. Weng, Z. Fang, and X. Dai, Topological insulator to Dirac semimetal transition driven by sign change of spin-orbit coupling in thallium nitride, Phys. Rev. B **90**, 245308 (2014).

[67] Z. Wang, Y. Sun, X.-Q. Chen, C. Franchini, G. Xu, H. Weng, X. Dai, and Z. Fang, Dirac semimetal and topological phase transitions in $A_3Bi(A = Na, K, Rb)$, Phys. Rev. B **85**, 195320 (2012).

[68] B.-J. Yang and N. Nagaosa, Classification of stable three-dimensional Dirac semimetals with nontrivial topology, Nat. Commun. **5**, 4898 (2014).

[69] See Supplemental Material at http://link.aps.org/supplemental/10.1103/PhysRevResearch.4.023127 for more details of the SOC Hamiltonian and the Zak phase in effective model, and the band structures as well as the TSC in $Ti(Se_{0.5}Te_{0.5})_2$.

[70] P. Hosur, P. Ghaemi, R. S. K. Mong, and A. Vishwanath, Majorana Modes at the Ends of Superconductor Vortices in Doped Topological Insulators, Phys. Rev. Lett. **107**, 097001 (2011).

[71] D. H. Lee and J. D. Joannopoulos, Simple scheme for surface-band calculations. I, Phys. Rev. B **23**, 4988 (1981).

[72] W. Liu, Q. Hu, X. Wang, Y. Zhong, F. Yang, L. Kong, L. Cao, G. Li, K. Okazaki, T. Kondo *et al.*, Tunable vortex Ma-jorana modes controlled by strain in homogeneous LiFeAs, arXiv:2111.03786.

[73] C. Caroli, P. D. Gennes, and J. Matricon, Bound Fermion states on a vortex line in a type-II superconductor, Phys. Lett. **9**, 307 (1964).

[74] F. Gygi and M. Schluter, Electronic tunneling into an isolated vortex in a clean type-II superconductor, Phys. Rev. B **41**, 822 (1990).

[75] C.-K. Chiu, P. Ghaemi, and T. L. Hughes, Stabilization of Majo-rana Modes in Magnetic Vortices in the Superconducting Phase of Topological Insulators using Topologically Trivial Bands, Phys. Rev. Lett. **109**, 237009 (2012).

[76] J. Zak, Berry's phase for energy bands in solids, Phys. Rev. Lett. **62**, 2747 (1989).

[77] S. Ryu and Y. Hatsugai, Entanglement entropy and the Berry phase in the solid state, Phys. Rev. B **73**, 245115 (2006).

[78] T. Shang, A. Amon, D. Kasinathan, W. Xie, M. Bobnar, Y. Chen, A. Wang, M. Shi, M. Medarde, H. Yuan *et al.*, Enhanced T_c and multiband superconductivity in the fully-gapped $ReBe_{22}$ superconductor, New J. Phys. **21**, 073034 (2019).